Deconvolved Image Restoration From Auto-Correlations

Daniele Ancora and Andrea Bassi

***Abstract*— The recovery of a real signal from its auto-correlation is a wide-spread problem in computational imaging, and it is equivalent to retrieve the phase linked to a given Fourier modulus. Image-deconvolution, on the other hand, is a fundamental aspect to take into account when we aim at increasing the resolution of blurred signals. These problems are addressed separately in a large number of experimental situations, ranging from adaptive astronomy to optical microscopy. Here, instead, we tackle both at the same time, performing auto-correlation inversion while deconvolving the current object estimation. To this end, we propose a method based on *I*-divergence optimization, turning our formalism into an iterative scheme inspired by Bayesian-based approaches. We demonstrate the method by recovering sharp signals from blurred auto-correlations, regardless of whether the blurring acts in auto-correlation, object, or Fourier domain.**

***Index Terms*— Deconvolution, phase retrieval, computational imaging, auto-correlation inversion, deblurring, inverse problem.**

I. Introduction

DECONVOLUTION is an image processing technique with extensive usage in computer vision and optics [1], [2], including astronomy [3] and optical microscopy [4]. Its goal is the restoration of super-resolved features of objects [5] imaged with diffraction-limited optics or aberrated wavefronts. Conversely, another class of inversion techniques in computational imaging deals with the estimation of an object given its auto-correlation. The latter is becoming a popular topic in recent years, thanks to the increased computational power available at the user level. This led to the implementation of fast reconstruction protocols in unconventional imaging scenarios, giving rise to a multitude of techniques. Applications based on auto-correlation imaging can be found in -but are not limited to- image detection through a turbulent medium (e.g. the atmosphere) [6], lens-less imaging [7], hidden imaging [8], and tomography [9]. Typically, to form a reconstruction of the object acquired in such conditions, one needs to invert the auto-correlation of the signal. Since this forms a pair with the modulus of the Fourier transform of the object, the image reconstruction process is often referred to as the phase-retrieval (PR) problem. Given that it is not possible to measure the phase directly with camera-sensors, PR tries to find it by constraining the reconstruction to be real and to have a given Fourier modulus [10]. There are several ways to approach this inverse problem that inspired many computational strategies: alternating projections, distance optimization, or iterative approaches embrace the vast majority of methods available. Although the field is in continuous progress, Shechtman *et al.* provides an extensive review on the topic [11].

However, even in this case, the finite bandwidth of the diffraction-limited detection system may blur the estimation of the object auto-correlation. Hence, if we want to achieve sharp reconstructions, we are left with the necessity to tackle two consecutive inverse problems (deconvolution and phase retrieval). Here, instead, we propose an iterative procedure to obtain a deconvolved image directly from auto-correlation measurements, solving both problems at the same time. We start by noticing that the blurred auto-correlation is equivalent to the target-object convolved by a kernel, which depends on the object itself. Inspired by blind deconvolution strategies [12], we discuss how neglecting the kernel's dependence on the object does not alter reconstruction abilities. We establishes our method by minimizing the *I*-divergence, similarly to Richardson-Lucy (RL) [1], [2] deconvolution algorithm and in close analogy with Schultz-Snyder (SS) approach [13]. Like other expectation-maximization (EM) protocols in signal processing, the algorithm can be further improved by adding total-variation regularization [14] or deconvolution with unknown kernels [12].

In the following section II, we start introducing the general problem-framework, contextualizing its applicability in different measurement-scenarios. In Sec. III, we introduce the iterative algorithm that solves both the auto-correlation inversion and the deconvolution problem. Sec. IV presents the reconstruction results and examines the deconvolution ability of the technique. After having introduced and described the method, in Sec. V we compare it against existing methodologies and -furthermore- we propose an experimental validation in the context of hidden auto-correlation imaging in Sec. VI. The last section VII concludes the study, discussing potential implementation and future ideas to continue its development.

December 04, 2020

II. Problem Statement

First of all, let's define the formalism that we will use throughout the manuscript. We will make use of integral formulations, keeping in mind that we can turn each equation

Manuscript received July 4, 2020; revised November 2, 2020 and December 1, 2020; accepted December 4, 2020. Date of publication December 14, 2020; date of current version December 23, 2020. The associate editor coordinating the review of this manuscript and approving it for publication was Prof. Lisimachos P. Kondi. *(Corresponding author: Daniele Ancora.)*

Daniele Ancora is with the Department of Physics, Politecnico di Milano, 20133 Milan, Italy (e-mail: daniele.ancora@polimi.it).

Andrea Bassi is with the Department of Physics, Politecnico di Milano, 20133 Milan, Italy, and also with the Istituto di Fotonica e Nanotecnologie, Consiglio Nazionale delle Ricerche, 20133 Milan, Italy.

Digital Object Identifier 10.1109/TIP.2020.3043387

into its discrete equivalent by replacing the integral with a summation over the integrated variables. For the sake of notation, we use one-dimensional functions of the spatial variable x, eventually shifted by the quantity ξ when calculating convolution or correlation operations. This formalism can be extended to any dimensionality, so we drop any explicit variable dependence. The operator $\mathbf{F}\{\ldots\}$ indicates the Fourier transform and the dot $\cdot$ implies the element-wise product. We indicate the cross-correlation between two generic functions $f(x)$ and $g(x)$ as:

$$f \star g = \int \overline{f(x)} g(\xi + x)\, dx = \mathbf{F}^{-1}\left\{\overline{\mathbf{F}\{f\}} \cdot \mathbf{F}\{g\}\right\}. \quad (1)$$

Consequently, the auto-correlation of the function f with itself is $f \star f$. The convolution is defined as:

$$f * g = \int f(x)\, g(\xi - x)\, dx = \mathbf{F}^{-1}\left\{\mathbf{F}\{f\} \cdot \mathbf{F}\{g\}\right\} \quad (2)$$

and the auto-convolution as $f * f$. In general, we are interested in the reconstruction of an unknown object o. Its auto-correlation is defined as:

$$\chi = o \star o = \mathbf{F}^{-1}\left\{\|\mathbf{F}\{o\}\|^2\right\}. \quad (3)$$

The identity on the right-hand side of Eq. 3 is given by the Wiener–Khinchin power spectrum theorem.

Throughout the text, we will make use of the greek-subscript μ when referring to a simulated/experimental measurement: this indicates that the underlined quantity is blurred and subject to noise. To avoid confusion from now on, we make use of the word "measurement" when referring to a simulated effect that may be observed in a real imaging experiment. The only exception is in the last part of section VI, where we refer to a real camera detection from an experimental measurement. In the present paper, we address the cases in which the auto-correlation is blurred, computed using a blurred object, or in which the measurement was performed in a band-limited Fourier space. Although slightly different, we report that these problems are equivalent and we can approach them all with the same iterative method.

A. Blurred Auto-Correlation

In some applications, we have access to a statistically computed estimate of the auto-correlation. Looking through turbulent atmosphere in astronomy [6], through scattering slabs or behind corners [8], [15] and performing hidden tomography [9] are just a few examples of that. The light that propagated in these conditions has undergone unpredictable scattering events and, when detected, resembles a random arrangement of the intensity distribution. Under isoplanatic conditions (also known as "memory effect" regime [16]) it has been proven that the auto-correlation of this pattern closely matches that of the object. To simplify, the turbidity acts as an opaque auto-correlation lens. To estimate the auto-correlation of the hidden object, we can use the pattern produced by the light propagation through the turbid environment. Since the auto-correlation is typically averaged through several detections, each of which is affected by blurring, the presence of an effective point-spread function (PSF) blurs the final estimate of

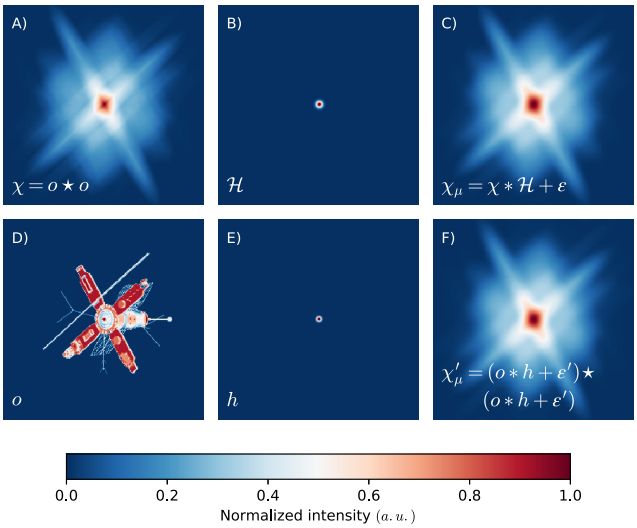

Fig. 1. A) Auto-correlation of an ideal object $\chi = o \star o$. Panel B) Gaussian kernel $\mathcal{H}$ with standard deviation $\sigma = 2\, px$ used to blur the auto-correlation. C) Auto-correlation χ_μ corrupted by Poissonian noise ε and blurred by $\mathcal{H}$. χ_μ reproduces the quantity that we can compute or measure in an auto-correlation experiment. D) Noise-free test image o of a satellite [19] used to test the reconstruction protocol (size $256 \times 256\, px$). E) Gaussian kernel h used for blurring the object. F) Auto-correlation χ'_μ calculated by using a blurred and noisy object. All the images are peak-normalized and displayed using a diverging color-map (reversed *RdBu*). .

the auto-correlation. Thus, we have access to a measurement of the auto-correlation given by:

$$\chi_\mu = \chi * \mathcal{H} + \varepsilon, \quad (4)$$

where $\mathcal{H}$ is a blurring kernel for the original object auto-correlation $\chi = o \star o$. Figure 1 shows the test image of a satellite o (panel D) used in this study, and its corresponding auto-correlation χ (panel A). We consider the case in which the image is blurred by a Gaussian kernel $\mathcal{H}$ (panel B) and leads to a noisy measurement of χ_μ (panel C). Usually these measurements benefit from the use of ensemble [17] averages or comes from photon differencing [18]; thus, for the moment, we consider ε as a generic form of additive noise. Approaching this problem would initially require the deconvolution of the auto-correlation (i.e. using Richardson-Lucy [1], [2]) and, then, to find the signal that generated it (e.g. by using Fienup iterative phase retrieval [10]), or vice versa. For completeness, Sec. V compares our method with standard ones and Sec. VI tests it in an experimental application.

Since we want to approach both problems simultaneously, we reduce the formula above to the convolutional form $o * \mathcal{K}$, where the object of interest o is subject to the blurring kernel $\mathcal{K}$. Let's rearrange the correlations and convolutions in a convenient form:

$$\begin{aligned} \chi * \mathcal{H} &= (o \star o) * \mathcal{H} = o \star (o * \mathcal{H}) \\ &= o \star (\mathcal{H} * o) = (o \star \mathcal{H}) * o \\ &= o * (o \star \mathcal{H}) \equiv o * \mathcal{K}, \end{aligned} \quad (5)$$

where we used the fact that convolution between two functions f and g permutes, $f * g = g * f$, and the correlation-convolution identity $(f \star g) * h = f \star (g * h)$.

In this way, we have introduced a new blurring kernel that depends on the object itself $\mathcal{K}[o] = o \star \mathcal{H}$. The convolution of the object with $\mathcal{K}$ gives the measured auto-correlation under the effect of a blurring factor $\mathcal{H}$.

B. Blurred Auto-Correlation Induced by Object-Blurring

The broad field of computed tomography (CT) gathers together many imaging protocols that let us to virtually inspect the features inside of the specimen of interest. Although there exist several techniques approaching the problem with different experimental designs, they share similar numerical pipelines for the reinterpretation of the results. In particular, deconvolution and alignment procedures are crucial tasks to obtain faithful reconstructions in CT. Auto-correlations, by definition, are centered in the shift-space so it is easy to reconstruct a tomographic auto-correlation starting from its projection sequence [20] by computing an auto-correlation sinogram. The inversion of the latter would return an exact reconstruction of the object with no prior alignment procedure applied. Still, this reconstruction is affected by blurring and needs to be treated accordingly to achieve a sharp result. In alignment-free tomography, we thus often rely on the computation of a blurred version of the auto-correlation χ_μ as in:

$$\chi'_\mu = \left(o * h + \varepsilon'\right) \star \left(o * h + \varepsilon'\right), \tag{6}$$

where the additive noise ε' perturbs the detection of each blurred projection of the object o. By dropping the noise term, it is possible to rearrange the problem to reach the same form as Eq. 5:

$$\begin{aligned}(o * h) \star (o * h) &= (o \star o) * (h \star h) \\ &= (o \star o) * \mathcal{H} \\ &= \chi * \mathcal{H},\end{aligned} \tag{7}$$

where the definition of $\mathcal{H} = h \star h$ makes the problem identical to Eq. 5. In this case, the convolutional kernel becomes $\mathcal{K} = o \star (h \star h)$. Equations 6-7 imply that the problem is symmetric, thus starting from a blurred auto-correlation it is possible to first deblur and then de-autocorrelate, or the other way around. However, as previously stated, we are interested in performing both actions at the same time. Further details concerning the presence of noise are discussed in the appendix A.

C. Blurring Due to Band-Limited Fourier Measurement

Let us consider the case in which we are performing a Fourier measurement limited by a generic window function W, as in coherent [21] or partially coherent [22] diffraction imaging (CDI). In these experiments, the detector acquires the squared modulus of the Fourier transform of the object, while it is not possible to access the phase information due to electronic limitations. Given that the phase of an electromagnetic signal is not measurable, imaging is usually accomplished by solving a phase retrieval problem [11] which has its Fourier modulus as a fixed constraint. The signal detected under these conditions can be expressed as:

$$\mathcal{M}_\mu = \|\mathbf{F}\{o\}\|^2 \cdot W + \varepsilon'', \tag{8}$$

where we introduced the window function to describe the limited size of the detector, which inevitably cuts some high spatial frequencies. By computing the auto-correlation from the sole measurement of $\mathcal{M}_\mu$, we have that:

$$\chi''_\mu = \mathbf{F}^{-1}\{\mathcal{M}_\mu\}, \tag{9}$$

where we used the Wiener-Kinchin power-spectrum theorem. We reach a formulation similar to Eq. 5 by making use of the convolution theorem:

$$\begin{aligned}\mathbf{F}^{-1}\{\|\mathbf{F}\{o\}\|^2 \cdot W\} &= \mathbf{F}^{-1}\{\mathbf{F}\{\chi\} \cdot \mathbf{F}\{\mathcal{H}\}\} \\ &= \mathbf{F}^{-1}\{\mathbf{F}\{\chi * \mathcal{H}\}\} \\ &= \chi * \mathcal{H}.\end{aligned} \tag{10}$$

Here, for the band-limited Fourier measurements, the convolution kernel reduces to $\mathcal{K} = o \star \mathbf{F}^{-1}\{W\}$. This result for the auto-correlation is analogous to the convolutional blurring in a band-limited measurement, as dictated by the limited aperture of a detection objective. The convolutional kernel is, in fact, a filter in the frequency domain. So far, we considered the effect of the noise to be negligible, but we provide a thorough discussion on the topic in the appendix A.

III. Iterative Method

As discussed in the previous section, several measurements fall within the same class of inverse problems that involve the inversion of the auto-correlation coupled with the simultaneous deconvolution of the reconstruction. Similarly to auto-convolution inversion [23], the problem examined can be generalized as a convolution with an effective kernel, which contains the object itself correlated with a blurring factor $\mathcal{H}$. In our formalism, $\mathcal{H}$ retains the description of the problem that we are interested in, among the three classes examined in section II. Before stepping further, let's introduce an approximation by dropping the explicit functional dependence on o from $\mathcal{K}[o] \rightarrow \mathcal{K}$. This approximation implies the complete knowledge of the convolution kernel: we will motivate this choice in the following paragraph.

Let us call a generic measurable distance between χ_μ and χ^* as $d\left(\chi_\mu || \chi^*\right)$, where $\chi^* = o^* * \mathcal{K}$ is the best estimate of the auto-correlation. Provided that χ_μ is the measurement, the optimal object's reconstruction o^* is reached when such distance $d\left(\chi_\mu || \chi^*\right)$ is minimized. Thus, the reconstruction problem turns into:

$$o^* = \arg\min d\left(\chi_\mu || \chi^*\right). \tag{11}$$

To satisfy the equation above, a necessary -but not sufficient- condition is given by setting to zero the functional derivative with respect to the object to be optimized o^*:

$$\frac{\delta}{\delta o^*} d\left(\chi_\mu || \chi^*\right) = 0. \tag{12}$$

There are several possible choices for $d\left(\chi_\mu || \chi^*\right)$, each of which would turn the search for the reconstruction into a different inverse problem. We deal with intensity measurements and it is therefore desirable that $o(x) \geq 0, \forall x$. To comply

with the positiveness of the solution, we chose the Csiszár's I-divergence [24] as distance estimator:

$$I\left(\chi_\mu||\chi^*\right) = \int \left\{\chi_\mu(\xi)\ln\left[\frac{\chi_\mu(\xi)}{\chi^*(\xi)}\right] + \chi^*(\xi) - \chi_\mu(\xi)\right\} d\xi. \quad (13)$$

Such quantity is a generalization of the relative entropy, known as Kullback-Leibler distance. This measure is common in iterative convolution/correlation inversion schemes [13], [23], whereas choosing the Euclidean norm $d\left(\chi_\mu||\chi^*\right) = \|\chi_\mu - \chi^*\|^2$ would usually turn the reconstruction into a least-square problem (see [3] for a thorough overview). We calculate the functional derivative of the I-divercence with respect to the optimal reconstruction o^*:

$$\frac{\delta}{\delta o^*} I\left(\chi_\mu||\chi^*\right) = -\frac{\delta}{\delta o^*}\int \left\{\chi_\mu \log\left[\chi^*(\xi)\right] - \chi^*(\xi)\right\} d\xi = \int \left(1 - \frac{\chi_\mu}{\chi^*(\xi)}\right)\frac{\delta}{\delta o^*}\left[\chi^*(\xi)\right] d\xi. \quad (14)$$

By setting it to zero and inserting the functional derivative calculated in the appendix B (Eq. 30), we obtain:

$$\int \left(1 - \frac{\chi_\mu}{\chi^*(\xi)}\right)\mathcal{K}(\xi - x)\, d\xi = 0. \quad (15)$$

We cannot provide a general closed solution for Eq. 15, but we can estimate an approximated one by using Picard's iterative-scheme [25]. The latter uses a fixed-point iterative formulation:

$$o^{t+1}(x) = o^t(x)\ \lambda^t(x), \quad (16)$$

where the updating rule $\lambda^t(x)$ is:

$$\lambda^t(x) = \int \frac{\chi_\mu(\xi)}{\int o^t(x)\,\mathcal{K}(\xi - x)\, dx}\mathcal{K}(\xi - x)\, d\xi. \quad (17)$$

The theory above is related to the expectation-maximization (EM) approach often used in similar procedures [26]. Using Csiszár's I-divergence guarantees that Eq. 16 converges to its minimum while keeping o^{t+1} subject to non-negative constraints. Seminal works in the field [23], [26], [27] further discuss details and properties of this approach.

It is worth noting that Eq. 17 is rigorous when $\mathcal{K}$ is fully determined and closely relates to RL-like schemes. However, similarly to the case of blind deconvolution [28], we do not have access to an exact estimate for $\mathcal{K}$. In blind-RL schemes, the point spread function (PSF) is updated via RL-steps, using the current object estimate as to the (transiently fixed) kernel that blurs the recorded image [12]. Here, instead, we decide to anchor the update (AU) of this kernel with the current estimate of the object, inferring a refined kernel at each step of the form:

$$\mathcal{K}_{AU}(\xi) = \int \overline{o^t(x)}\mathcal{H}(x + \xi)\, dx. \quad (18)$$

In a compact convolutional notation, the whole iterative AU-process becomes:

$$\mathcal{K}^t_{AU} = o^t \star \mathcal{H} \quad (19)$$

$$o^{t+1} = o^t\left[\left(\frac{\chi_\mu}{o^t * \mathcal{K}^t_{AU}}\right) * \widetilde{\mathcal{K}}^t_{AU}\right] \quad (20)$$

where $\widetilde{\mathcal{K}} = \mathcal{K}(-x)$ denotes reversed axis. The convolutional kernel is refined at each iteration, taking into account the previous object estimate and used to deblur the auto-correlation into the new object reconstruction o^{t+1}. In the particular case of $\mathcal{H} = \delta$, the problem is not reduced to the deauto-convolution method as one would think [23], since $\mathcal{K}_\delta = o \star \delta = \overline{o(-x)}$. For ease of notation, we do not use normalization constants, assuming all the quantities to be energy-normalized before processing. This procedure guarantees the conservation of the total intensity throughout the minimization.

IV. Reconstruction Results

In order to test the reconstruction protocol, let's define a metric to assess the quality of the images obtained. Given a generic measured signal corrupted by additive noise, $s_\mu = s + \varepsilon$, we estimate the fidelity of the measurement against the noiseless signal with the signal-to-noise ratio (SNR):

$$\mathrm{SNR}\left(s_\mu\|s\right) = 20\log_{10}\left[\frac{\int s_\mu\, dx}{\int\left(s_\mu - s\right) dx}\right] \quad (21)$$

$$\mathrm{SNR}\left(s_\mu\|\varepsilon\right) = 20\log_{10}\left[\frac{\int s_\mu\, dx}{\int \varepsilon\, dx}\right]. \quad (22)$$

These equivalent forms are commonly used for intensity detection and expressed in decibel, dB. In the cases examined, s (and s_μ) might stand either for the auto-correlation χ (and χ_μ) or for the object o (and o_μ).

A. Reconstruction From a Blurred Auto-Correlation

We start our analysis by discussing the results of the AU on the image of the satellite, subject to the experimental conditions described in section II-A. Thus, we want to reconstruct the object o^* from the auto-correlation $\chi_\mu = \chi * \mathcal{H} + \varepsilon$. We start with χ having 16-bit accuracy, to which we add a random Poissonian noise with different parameters $\lambda = 2^{12}$, 2^8 and 2^4. For a Poisson distribution, we recall that λ corresponds both to the mean value and to the variance. To quantify the effect of the noise on the measured signal, we use the SNR as defined in Eq. 22. Here, we consider a Gaussian point-spread function h with standard deviation $\sigma = 2\,px$, defining the blurring kernel for the auto-correlation as $\mathcal{H} = h * h$. The quantity $\mathcal{H}$ is also a Gaussian, having a broader $\sigma = 4\,px$. Adding Poissonian noise (with the λ defined above) to the blurred object auto-correlation, $\chi * \mathcal{H}$, results into three different $\mathrm{SNR}\left(\chi_\mu\|\varepsilon\right) = 2.6\,dB$, $26.7\,dB$ and $50.8\,dB$ for the χ_μ. For the post-processing, we subtract the mean of the noise to the auto-correlation, then we take its absolute value since negative correlation would be unphysical for the reconstruction of an intensity image. After this, we normalize by dividing for its total intensity. As from the problem statement, we know the generic blurring function $\mathcal{H}$ and we start from a strictly positive initial guess of the object $o^{t=0} = o^i$, energy-normalized so that $\int o^t(x)\, dx = 1$. In principle, o^i could accommodate any known prior, such as information about sparsity or a low-resolution estimate of the object, if available. However, we assume the object to be completely unknown, feeding a random initial guess to the AU-iterations.

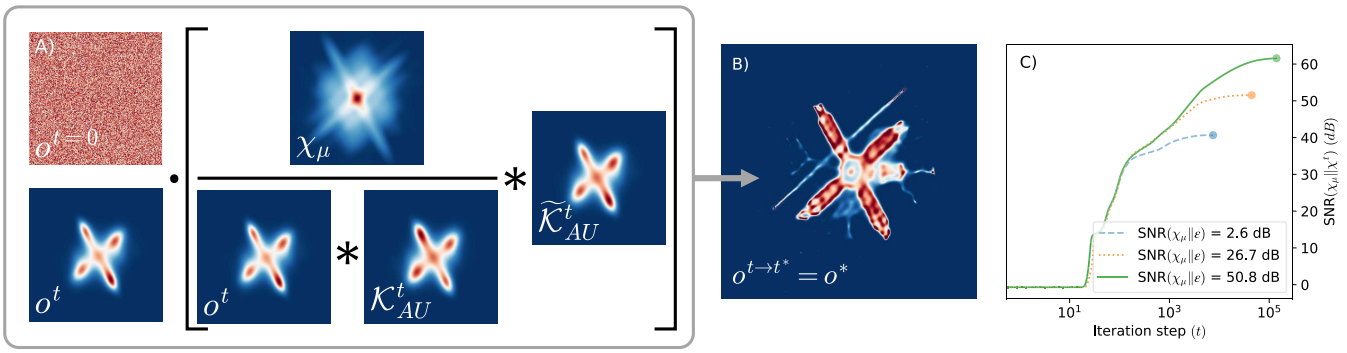

Fig. 2. Panel A) shows a schematic of the AU iteration, as in Eq. 20. A random guess is chosen as the starting point for $t = 0$, and then the results after $t = 60$ iterations are displayed. Panel B) visualizes the result after around 10^5 iterations of the deblurred auto-correlation inversion subject to Poissonian noise $\lambda = 2^4$. This reconstruction refers to section IV-A. In C), the plot relative to the SNR during the iteration steps for all the noises examined in the present study.

Fig. 2 presents a view of the iterative scheme at $t = 60$ in the case of low-noise, where it appears evident the formation of a blurred version of the satellite. Since AU minimizes the I-divergence, we rely on the signal-to-noise ratio to monitor the reconstruction quality as the iteration progresses. We compute the SNR$(\chi_\mu\|\chi^t)$ as defined in Eq. 21, treating the current estimate for the (blurred) auto-correlation $\chi^t = o^t * \mathcal{K}^t_{AU}$ as a perturbation with respect to the given quantity χ_μ. Thus, the noise of the current auto-correlation estimate after t steps would be $\varepsilon^t = \chi_\mu - \chi^t$. While progressing, we expect that our method would increase the SNR until achieving an optimal point, after which the reconstruction quality degrades. Therefore, we stop the iteration when the SNR of the reconstruction becomes lower than the previous value. The plot in Fig. 2C shows the trend for the three noises considered, and the dots represent the stopping point for each reconstruction. The initial increase is similar for all cases, in general, but a low-noise measurement leads to a reconstruction with a higher SNR. This trend can be compared with the measured SNR$(\chi_\mu\|\varepsilon)$ since, in either case, it is calculated directly on auto-correlations.

B. Reconstruction From an Auto-Correlation of a Blurred Object

Here, we discuss the results in the case where the auto-correlation is obtained by a blurred estimate of the object, as in $\chi_\mu = (o * h + \varepsilon') \star (o * h + \varepsilon')$. This study refers to section II-B and we consider o acquired with 16-bit accuracy. The kernel h was chosen to be a Gaussian with standard deviation $\sigma = 2\,px$. The blurred object is perturbed by the addition of Poisson's noise with three different $\lambda = 2^{12}$, 2^8 and 2^4, as in the previous case. Here, the SNR of the measurement is referred to the measured object $o_\mu = o * h + \varepsilon'$, thus SNR$(o_\mu\|\varepsilon')$, rather than to its auto-correlation. Remarkably, in all cases, the AU-iteration converged to faithful reconstructions during an entire run of 10^6 iterations.

The results are shown in Fig. 3. Panel A displays the output result with SNR$= 6.3\,dB$, whereas panel B refers to SNR$= 25.2\,dB$ and panel C to SNR$= 48.8\,dB$. As expected, the results improve by reducing the noise, and fine details become visible for both the reconstructions in

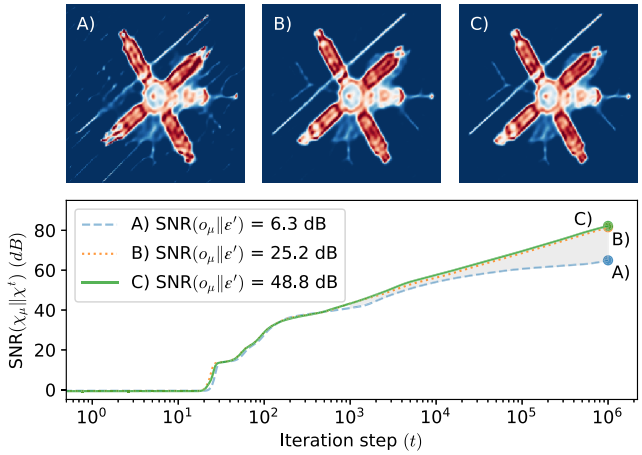

Fig. 3. Simulation results for the experiment described in section II-B. A) Output of the reconstruction after 10^6 iteration for the lowest SNR. B) Result for the intermediate SNR and C) for the highest. The bottom panel shows the plot of the SNR as a function of the iteration step (in log-scale).

panels 3B and 3C. In these cases, the quantity SNR$(o_\mu\|\varepsilon)$ cannot be directly compared with the values shown on the bottom graph, since it is referred to the object, not to the auto-correlation. We should compare, instead, the SNR$(\chi_\mu\|\chi * \mathcal{H})$ that turns to be $32.9\,dB$, $44.5\,dB$ and $56.6\,dB$ respectively for panels 3A, 3B and 3C. In this case, a seemingly good SNR$(\chi_\mu\|\chi * \mathcal{H}) = 32.9\,dB$ gives poor reconstruction quality (Fig. 3A), especially if compared to the one obtained in the previous section. This may be happening because additive noise in this experimental regime is transported into the auto-correlation in a non-trivial fashion, as discussed in the appendix A. However, these results are visually comparable to those obtained in the previous section.

It is worth noting that the problem treated here is equivalent to a classical deconvolution approach. To understand this, we focus on the dashed line profiles in Fig. 4. The original object o in panel A is compared against its blurred version $o_\mu = o * h + \varepsilon'$ (panel B) and with our reconstruction (panel C). The latter is aligned against the original object by finding the peak of their cross-correlation and translating the reconstruction accordingly. The results can be interpreted

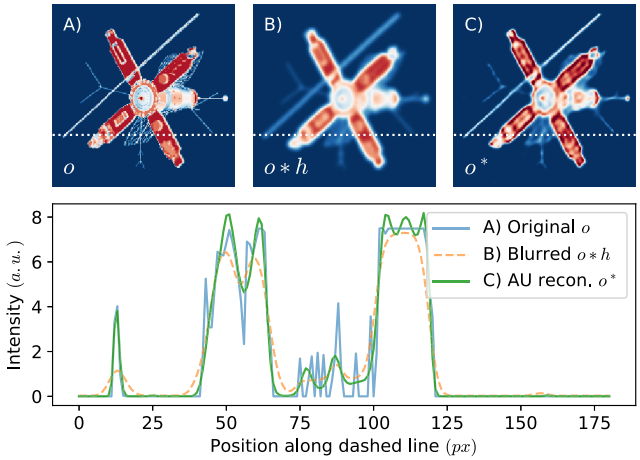

Fig. 4. Top row, profile comparison between the original object, shown in panel A), the blurred object B) as in $o * h + \varepsilon$ and the results of the AU algorithm C) for the experiment described in II-B. The dashed lines in A,B,C represent where, in the images, the profile was analyzed. The noise is generated using $\lambda = 2^8$. The plot at the bottom shows the profile through these directions in the images.

by focusing the analysis on the leftmost spike in the plot of Fig. 4. We notice that the smooth-peak (orange dashed) is sharpened by the AU iterations (green line), approaching the resolution of the original object (blue line, reference). Along this profile, the recovered intensity exceeded the expected value in the central region (over-shoot): this might happen also with RL-deconvolution that preserves the overall energy, but local fluctuations may alter the reconstructed values. The same concept applies to all the features in the image, as can be seen by a more accurate analysis of the plot. In particular, the flat region on the right side of the plot exhibits oscillations (under- and over-shoot) around the correct value. These results suggest that AU is inverting an auto-correlation sequence, deblurring the reconstruction at the same time. However, our method is not meant to be an alternative to standard deconvolution. In the case of single real-space acquisitions, a deconvolution approach is still the appropriate option for image-deblur. On the other hand, one could encounter situations in which the object is not visible as a whole [29], [30] and the sample needs to be measured from different perspectives. This situation typically requires an alignment or co-registration procedure of each view to form the reconstruction. Here, protocols based on auto-correlation inversion may lead to alternative reconstruction strategies since auto-correlations are inherently aligned to the shift-space origin.

V. Comparison With SS-RL Mixed Approach

The AU method is capable of inverting the auto-correlation and simultaneously deconvolving the reconstruction. So far, we have tested it under different measurement conditions, obtaining faithful reconstructions. However, it is worth comparing it against other methods used in the literature, briefly discussing its applicability in an experimental scenario. In the following, we test AU reconstructions against standard deauto-correlation and deconvolution methods, using similar working conditions for each protocol. Our method starts from an auto-correlation sequence that we assume to be blurred by the kernel $\mathcal{H}$. For this comparison, we consider once again Poisson noise with $\lambda = 2^4$ and a Gaussian kernel h with $\sigma = 2$. Since AU was developed to tackle both tasks simultaneously, we have to split the comparing pipeline into deconvolution and auto-correlation inversion. The latter falls within the realm of the phase-retrieval problems where, given the Fourier modulus of the object, we want to reconstruct its underlined phase. A gold-standard approach to the PR problem is to use alternating-projection schemes proposed by Fienup [10]. We initially approached the problem by implementing a standard combination of hybrid input-output (HIO) and error reduction (ER) strategies. We spoil the results right ahead: PR combined with RL deconvolution always turned into poor-quality reconstruction.

Each inversion strategy comes with its artifacts that do not behave well when concatenated with different methods. In particular, PR that uses alternating projections apply sharp thresholds back and forth between the real and Fourier space that may lead to unpredictable behavior where the signal is low [31]. Instead, Schultz-Snyder's method entirely operates in the spatial domain, alike our AU extension. Thus, a smooth comparison has to involve the usage of the Richardson-Lucy's (RL) algorithm for the deconvolution and Schultz-Snyder's (SS) to invert the auto-correlation since both optimize the same I-divergence metric. Clearly, even if the kind of metric optimized is the same, the divergence minimized by RL is that of a linear problem in o, while SS and AU attempt to work out a quadratic problem.

To begin with, we perform a deconvolution, then we invert the auto-correlation (RL then SS). Conversely, we also test the reverse procedure, inverting the auto-correlation and then deconvolving the result (i.e. applying SS then RL). As discussed in II-B for $\mathcal{H} = h \star h$, the convolution and auto-correlation operators commute and both procedure should be equivalent. AU and SS are the same class of algorithm and have a slow convergence rate, so we consider the case of running $N_{AU} = N_{SS} = 10^4$ iterations. RL typically converges faster than SS, so an excessive number of iterations may enhance artifacts: we set $N_{RL} = 10^2$ iterations. For the first test (displayed on the first row of Fig. 5), we run RL on the auto-correlation and then SS on the result. Visually, the deconvolved auto-correlation resembles the expected auto-correlation χ as in Fig. 1A, with the reddish-core shrunk back similarly to its not-blurred counterpart. However, the reconstruction obtained inverting this auto-correlation exhibits the presence of artifacts. On the contrary, the second row in Fig. 5 shows the output after running an initial set of SS iterations on χ_μ, which is later deblurred by h via RL steps. The plot on the first panel of the second row shows an increasing trend for the auto-correlation SNR solely for the SS and AU methods (RL measures it against the actual object). The profile-plot on the bottom row of Fig. 5 compares the reconstructed intensities against each other. In either case of panels C and E, the final reconstruction is loaded with artifacts, particularly if compared with the result of our AU-method in panel F. The number of iteration for each protocol is a crucial parameter to fine-tune if we want smoothly move to the next inverse problem. The large plethora of combinations available

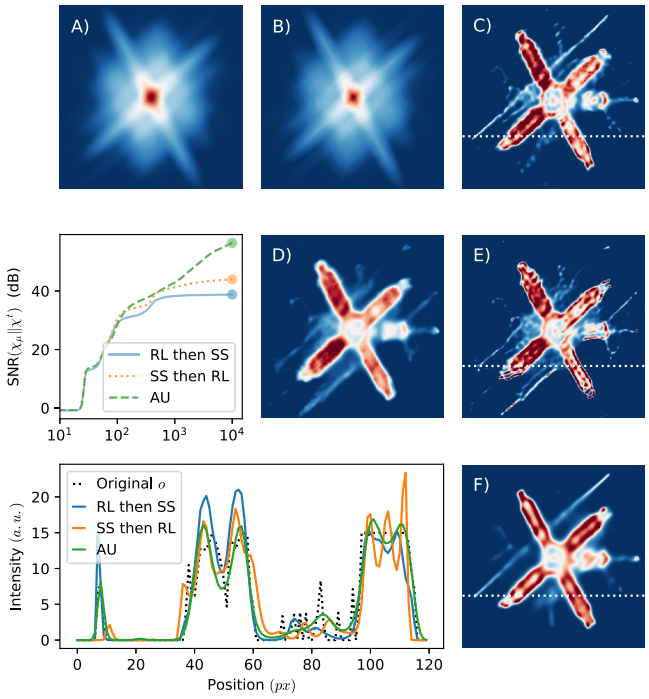

Fig. 5. Comparison of mixed SS-RL approaches against AU. A) The measured blurred auto-correlation χ_μ corrupted with noise. This is the starting point for each of the three cases examined. B) Deblurred reconstruction of the auto-correlation via RL. C) Deauto-correlated reconstruction after SS iterations. D) Result obtained inverting blurred auto-correlation with SS and E) deconvolved result. F) Direct deblurred and deauto-correlated reconstruction obtained with the AU method developed in this work. The plot in the second row monitors the SNR for the SS and AU algorithms. The plot on the bottom row shows a profile along the dashed line in panels C, D, and F. The dashed black curve in the plot is the profile of the original image o, taken from Fig. 4A. Here it serves as the ground truth for the reconstructions.

for the mixed models leaves the user with the necessity to look for the best sequence of iterations for both RL and SS, together with an appropriate choice of two starting guesses. The design of AU helps in this respect, having just one parameter to set (N_{AU}) to ensure the accomplishment of deconvolution and deauto-correlation at the same time. In principle, we cannot exclude that a perfect combination of iterations for RL and SS may lead to better reconstructions. However, we found that incorporating both aspects within the same inversion behave more robustly than concatenating two different problems.

VI. Reconstruction in Experimental Hidden Imaging

So far, we have performed numerous numerical experiments on synthetic datasets corrupted by Poissonian noise. To finalize our study, we put AU in action by working out reconstructions in a challenging experimental imaging scenario. This test serves as an experimental proof-of-concept of its application for the solution of real problems.

Let us consider the case in which we want to image an object hidden behind a random medium, subject to memory effect isoplanatism [8]. Experimental imaging in these conditions typically deals with the reconstruction of an unknown incoherently-emitting sample hidden behind an opaque diffuser. In this context, we are not interested in the imaging procedure per se: we refer to relevant literature on the topic for further details [8], [15]. For our purpose, we need to consider that the light emerging from a random surface has undergone unpredictable -yet deterministic- scattering events. This gives rise to the formation of a seemingly random speckle pattern s_μ, determined by the convolution between the random (and usually unknown) point response of the system h_s and the hidden object, as $s_\mu = o * h_s$. The pattern produced by the light that propagated through the obstacle can be recorded by placing a camera detector in front of the diffuser. No optics are generally involved in these imaging setups. The speckle s_μ shown in Fig. 6A represents a typical detection under these conditions: here, we are interested to study how our algorithm behaves in this case study. The pattern was generated by hiding a number "4", isolated from a USAF test target, behind a ground-glass diffuser and was taken from the work of Wu *et al.* [32], to which we refer to for experimental details. Before stepping further, we perform flat field correction by dividing the camera detection by its low-pass version (Gaussian smoothed with $\sigma = 50$) and then we subtract the mean value of the resulting pattern. It is a standard preprocessing pipeline for the best estimation of the auto-correlation in speckle imaging. In these conditions, χ_μ closely resembles the one of the hidden object itself (panel B), and imaging is accomplished typically by solving a Fienup-like phase retrieval problem [15] or via bispectrum analysis [32]. Following the theoretical framework for hidden imaging, we have that:

$$\begin{aligned}\chi_\mu &= s_\mu \star s_\mu \\ &= (o * h_s) \star (o * h_s) \\ &= (o \star o) * (h_s \star h_s) = \chi * \mathcal{H}_s,\end{aligned} \tag{23}$$

where h_s is the speckle pattern ideally produced by a single point source laying at the object plane. Since we do not have access to the object plane by hypothesis, h_s is not directly measurable and strictly depends on the observation point of the camera with respect to the scattering slab. When the randomized scrambling process is fully developed, however, $\mathcal{H}_s$ can be calculated theoretically and depends on the parameters of the system:

$$\mathcal{H}_s = 4\left[\frac{J_1\left(\pi\, Dr/\lambda v\right)}{\pi\, Dr/\lambda v}\right]^2. \tag{24}$$

Here, J_1 is a Bessel function of the first kind, D the pupil of the system, r the radial coordinate, λ the wavelength, and v the image distance. In this situation, then, $\mathcal{H}_s$ blurs the object's auto-correlation directly and does not depend on which portion of the turbid slab is illuminated.

Currently, to deal with the problem of the reconstruction of a sharp object o from speckle acquisition, an intricate sequence of PR and RL is used to isolate h_s from s_μ [33]. Here we do not solve the PR. Instead, we make use of SS to reconstruct a blurred version of the hidden object, comparing the result with that of our AU method. Experimentally, both methods converge after approximately 10^3 iterations. The hidden "4" taken from the USAF test target was correctly retrieved by either SS, in panel C, and AU, in panel D, of Fig. 6. Due to the

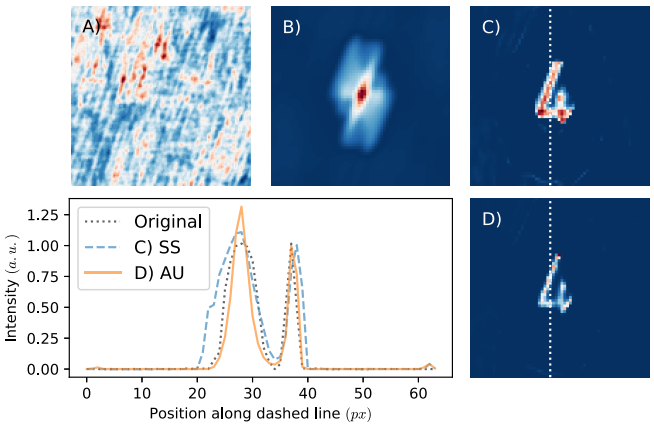

Fig. 6. Deconvolved image restoration from hidden measurements. A) Speckle pattern s acquired by [32] hiding an object o behind an opaque diffuser. B) Auto-correlation of the speckle pattern. C) Reconstruction of the object obtained by applying SS on the auto-correlation. D) Reconstruction with AU considering the theoretical auto-correlation PSF $\mathcal{H}_s$. The plot-profile along the dashed lines in panels C and D shows the deblurring effect of using our AU method with respect SS. The dashed curve, instead, is taken from the original object acquired with an objective lens, and serves as reference for the reconstructions. The curves are normalized with respect to the peak on the right side.

simultaneous deconvolution effect, the reconstruction obtained with our AU method is sharper with respect to the one derived with SS. Drawing a profile through the reconstructions (bottom row plot in Fig. 6) highlights the effect of the deconvolution, exhibiting narrower lines and preserving the overall shape of the reconstructed object. The experiments described above are preliminary results, further investigations are currently ongoing to explore the functionality of our method in optical microscopy, tomography, and hidden imaging.

VII. Conclusion

So far, we have discussed the problem of simultaneous deconvolution and auto-correlation inversion. Our approach was grounded on the theoretical basis of I-divergence optimization: the results from RL-deconvolution [1], [2], deauto-correlation [13] and deauto-convolution [23] strongly inspired the development of the present algorithm. We studied the reconstructions using auto-correlation that are directly blurred, calculated from a blurred object, or obtained with a band-limited detection. Here, we studied how to incorporate these inverse problems within the same formalism, proposing and testing the AU-algorithm as a reconstruction scheme. Remarkably, the method showed promising performances under a variety of experimental noise-levels, leading to faithful and robust reconstructions. Since the problem is similar to a phase retrieval process (with added deblurring), we expected the solution to be statistically sensitive to prior initialization [11]. As a matter of fact, the method behaved well in all the conditions tested, converging to visually similar reconstructions even with independent random initialization. Being the auto-correlation insensitive to the absolute positioning of the object, it is worth noting that any independent reconstruction grows randomly positioned in space. This is considered a trivial non-uniqueness connected with this class of inverse problems, as it is an inherent feature of the auto-correlation (and to the Fourier modulus of the object). Even if not explicitly mentioned, every reconstruction was realigned against the original object for visual comparison only. In fact, the Fourier phase encodes the information about the absolute position of the object, which shares the same class of shift-invariant solutions as in PR approaches [11]. Although interesting per se, this approach might have potential applications where ensemble averages are the sole (or the optimal) way for the estimation of the object auto-correlation. Imaging through turbulence [6], hidden imaging [8], or related problems, are scenarios where AU could be applied. As an experimental validation, we tested the AU method for the reconstruction of an object hidden behind opaque glass, obtaining a sharp and deconvolved reconstruction. This proof-of-concept paves the road for further investigations in the field of auto-correlation sensing, in which our method can find extensive usage. Furthermore, AU may allow further developments in the field of multi-view tomography [20] since the auto-correlation is insensitive to translations, and it can be easily estimated to neglect data-alignment procedures. Of course, similar schemes deal with the solution of a generic phase-retrieval problem that is well known to produce not stable results under various experimental conditions [10]. This is why we decided to approach the problem using a fix-point iteration scheme rather than including deconvolution in alternate-projection PR methods. The choice to optimize the I-divergence gives room also for further improvements by, for example, importing strategies developed in standardized deconvolution methods. Among the others, blind kernel updates [28], or total-variation regularization [14] are two features that we are considering to include in future developments of the AU protocol.

Appendix A
Noise in Cross-Correlation Problems

Since we have used the Csiszár's I-divergence, the ideal inversion-scenario happens when the signal is corrupted by Poisson noise. However, it has been proven that similar approaches behaved well in the case of high SNR measurements with experimental noise. Here we discuss, in all the cases, how detection noise can be related to the additive noise described in section II-A, where we had that $\chi_\mu = \chi * \mathcal{H} + \varepsilon$. Separating all the noise-terms in χ'_μ leads to:

$$\begin{aligned}\chi'_\mu &= \left(o * h + \varepsilon'\right) \star \left(o * h + \varepsilon'\right) \\ &= \chi * \mathcal{H} + (o * h) \star \varepsilon' + \varepsilon' \star (o * h) + \varepsilon' \star \varepsilon'. \quad (25)\end{aligned}$$

We can recognize that this expression matches with χ_μ when:

$$\varepsilon = (o * h) \star \varepsilon' + \varepsilon' \star (o * h) + \varepsilon' \star \varepsilon'. \quad (26)$$

For uncorrelated, random noise with uniform variance throughout the image, the last term reduces to $\varepsilon' \star \varepsilon' = \delta$. Furthermore, if the noise is not correlated with the signal $o * h$ itself, also the first two terms vanish when $\varepsilon' \to 0$. For the band-limited measurement considered in Eq. 9, it is easy to recognize that the noise is related to ε via:

$$\varepsilon = \mathbf{F}^{-1}\{\varepsilon''\}. \quad (27)$$

For random high-frequency additive noise, the formulation above implies that ε perturbs the auto-correlation as a strongly peaked function $\varepsilon \to \delta$, centered at the zero-shift space of the auto-correlation. In all the cases aforementioned, the noise does not diverge when computing the auto-correlations.

Appendix B
Partial Variational Derivative of χ^*

In this section, we consider the case study in which we ignore the explicit dependence of $\mathcal{K}[o]$ from o. This implies that we can estimate $\mathcal{K}$ as not being a functional form of o. As for the definition of variational derivative [34], we let the function o variate by a small amount $o + \epsilon\theta$ that implies:

$$\frac{d}{d\epsilon} F[o+\epsilon\theta]\Big|_{\epsilon=0} =: \int \frac{\delta F[o]}{\delta[o(x)]}\theta(x)\,dx. \tag{28}$$

If we apply this to the optimal auto-correlation χ^* that minimizes the I-divergence, dropping the asterisk in o^*, we have:

$$\begin{aligned}
&\frac{d}{d\epsilon}\chi^*[o+\epsilon\theta]\Big|_{\epsilon=0} \\
&= \frac{d}{d\epsilon}\int \left[\overline{o(x)} + \epsilon\overline{\theta(x)}\right]\mathcal{K}(x-\xi)\Big|_{\epsilon=0} dx \\
&= \frac{d}{d\epsilon}\int \epsilon\theta(x)\,\mathcal{K}(x-\xi)\Big|_{\epsilon=0} dx \\
&= \int \theta(x)\,\mathcal{K}(x-\xi)\,dx.
\end{aligned} \tag{29}$$

Sometimes, it is useful to identify the action of the variational derivative on a Dirac's delta function, that would let us rewrite:

$$\frac{\delta}{\delta[o(x)]}[o * \mathcal{K}] = \delta * \mathcal{K} = \mathcal{K}(\xi - x). \tag{30}$$

Let us notice that this is similar to the functional derivatives that, in Richardson-Lucy deconvolution, lead to a convolution with a reversed kernel [1], [2]. In our case, in contrast with the latter, the kernel does not remain stable during the whole minimization.

Appendix C
Complete Variational Derivative of χ^*

Here, we calculate the complete variational derivative of the auto-correlation. Again, we drop the asterisk in o^* and χ^* to denote the optimal estimation of the object and auto-correlation χ^*. For this task, let us consider that all the signals we are dealing with are real so that we do not treat explicitly complex conjugates. We have that:

$$\begin{aligned}
&\frac{\delta}{\delta[o(x)]}[o * \mathcal{K}[o]] \\
&= \left(\frac{\delta}{\delta[o(x)]}o\right) * \mathcal{K}[o] \\
&\quad + o * \left(\frac{\delta}{\delta[o(x)]}\mathcal{K}[o]\right).
\end{aligned} \tag{31}$$

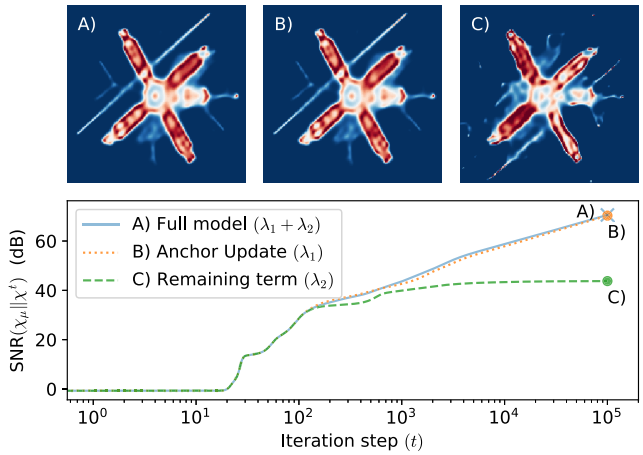

Fig. 7. Result comparison of: A) the full-model (updating with $\lambda_1^t + \lambda_2^t$), B) the AU approximation (update λ_1^t) and C) the remaining term (update λ_2^t) as described in Eq. 35. The plot at the bottom shows that making use of the AU approximation does not degrade the image quality achievable by the model, whereas the remaining term λ_2^t does not suffice reconstruction purposes.

The first term is identical to what obtained in the appendix B, the second, instead:

$$\begin{aligned}
&\frac{\delta}{\delta[o(x)]}\mathcal{K}[o] \\
&= \frac{\delta}{\delta[o(x)]}[o \star \mathcal{H}] \\
&= \left(\frac{\delta}{\delta[o(x)]}o\right) \star \mathcal{H} = \delta \star \mathcal{H}.
\end{aligned} \tag{32}$$

Here, the order of the terms is important since the correlation operator is not commutative. We have that:

$$\begin{aligned}
&\frac{\delta}{\delta[o(x)]}[o * \mathcal{K}[o]] \\
&= \delta * \mathcal{K} + o * (\delta \star \mathcal{H}) \\
&= \delta * \mathcal{K} + (\delta \star \mathcal{H}) * o \\
&= \delta * \mathcal{K} + \delta \star (\mathcal{H} * o)
\end{aligned} \tag{33}$$

To reach the formulation above, we have kept the Dirac's delta functions to take advantage of its correlation/convolution properties. Eq. 33 suggests that the correct update of the iterative method is:

$$o^{t+1} = o^t\left[\left(\frac{\chi_\mu}{o^t * \mathcal{K}^t}\right) * \widetilde{\mathcal{K}}^t + \left(\frac{\chi_\mu}{o^t * \mathcal{K}^t}\right) \star (o * \mathcal{H})\right] \tag{34}$$

$$= o^t\left[\lambda_1^t(x) + \lambda_2^t(x)\right]. \tag{35}$$

The update rule $\lambda^t(x)$ is now composed by two terms, in analogy with what found for the auto-correlation inversion by Schultz and Snyder in [13]. The first term $\lambda_1^t(x)$ can be recognized as the formulation given by the AU iteration in Eq. 20, instead, $\lambda_2^t(x)$ is a new term that enforces the update. We can test how much the result changes in case we consider: A) the full model given in Eq. 35, B) the AU iteration (obtained by setting $\lambda_2^t(x) = 0$) and C) using the remaining term only (where $\lambda_1^t(x) = 0$).

In figure 7, we report the results of the comparison carried on the numerical experiment described at II-A. From the plot in the bottom panel plot, we notice that the full model completes the run with the highest SNR, and the AU closely

performs, following a very similar trend. On the other hand, the remaining term started diverging from an ideal behavior after 10^2 iterations, slowly saturating the reconstruction's SNR. The output images of the full model in Fig. 7A and the AU in Fig. 7B are almost indistinguishable, whereas the remaining term returned a noisier image (Fig. 7C). In the latter image, we notice that the long antenna is formed both on the correct and on the wrong side. It is an indication that this approximation may suffer from a twin-image reconstruction problem, were the algorithm stagnates into a reconstruction given by the combination of the object o and its mirrored version $\widetilde{o}$. This is a well-known issue in the error-reduction PR method that stimulated further studies to overcome this algorithmic behavior [35]).

ACKNOWLEDGMENT

H2020 Marie Skłodowska-Curie Actions (HI-PHRET project, 799230); H2020 Laserlab Europe V (871124). The authors thank Prof. Antonio Pifferi for scientific and logistic support, Gianmaria Calisesi for inspiring discussions and Dr. Alessia Candeo for proofreading the article.

REFERENCES

[1] W. H. Richardson, "Bayesian-based iterative method of image restoration," *J. Opt. Soc. Amer.*, vol. 62, no. 1, pp. 55–59, Jan. 1972.
[2] L. B. Lucy, "An iterative technique for the rectification of observed distributions," *Astronomical J.*, vol. 79, p. 745, Jun. 1974.
[3] J.-L. Starck, E. Pantin, and F. Murtagh, "Deconvolution in astronomy: A review," *Publications Astron. Soc. Pacific*, vol. 114, no. 800, p. 1051, 2002.
[4] J.-B. Sibarita, "Deconvolution microscopy," in *Microscopy Techniques*. Berlin, Germany: Springer, 2005, pp. 201–243.
[5] E. A. Mukamel, H. Babcock, and X. Zhuang, "Statistical deconvolution for superresolution fluorescence microscopy," *Biophysical J.*, vol. 102, no. 10, pp. 2391–2400, May 2012.
[6] M. C. Roggemann, B. M. Welsh, and B. R. Hunt, *Imaging Through Turbulence*. Boca Raton, FL, USA: CRC Press, 1996.
[7] B. Abbey *et al.*, "Lensless imaging using broadband X-ray sources," *Nature Photon.*, vol. 5, no. 7, p. 420, 2011.
[8] J. Bertolotti, E. G. Van Putten, C. Blum, A. Lagendijk, W. L. Vos, and A. P. Mosk, "Non-invasive imaging through opaque scattering layers," *Nature*, vol. 491, no. 7423, p. 232, 2012.
[9] D. Ancora, D. Di Battista, A. M. Vidal, S. Avtzi, G. Zacharakis, and A. Bassi, "Hidden phase-retrieved fluorescence tomography," *Opt. Lett.*, vol. 45, no. 8, pp. 2191–2194, 2020.
[10] J. R. Fienup, "Phase retrieval algorithms: A personal tour," *Appl. Opt.*, vol. 52, no. 1, pp. 45–56, 2013.
[11] Y. Schechtman, Y. C. Eldar, O. Cohen, H. N. Chapman, J. Miao, and M. Segev, "Phase retrieval with application to optical imaging: A contemporary overview," *IEEE Signal Process. Mag.*, vol. 32, no. 3, pp. 87–109, Mar. 2015.
[12] D. Kundur and D. Hatzinakos, "Blind image deconvolution," *IEEE Signal Process. Mag.*, vol. 13, no. 3, pp. 43–64, May 1996.
[13] T. J. Schulz and D. L. Snyder, "Image recovery from correlations," *J. Opt. Soc. Amer. A, Opt. Image Sci.*, vol. 9, no. 8, pp. 1266–1272, 1992.
[14] N. Dey, L. Blanc-Feraud, C. Zimmer, Z. Kam, J.-C. Olivo-Marin, and J. Zerubia, "A deconvolution method for confocal microscopy with total variation regularization," in *Proc. 2nd IEEE Int. Symp. Biomed. Imag., Macro Nano*, Apr. 2004, pp. 1223–1226.
[15] O. Katz, P. Heidmann, M. Fink, and S. Gigan, "Non-invasive single-shot imaging through scattering layers and around corners via speckle correlations," *Nature Photon.*, vol. 8, no. 10, p. 784, 2014.
[16] I. Freund, M. Rosenbluh, and S. Feng, "Memory effects in propagation of optical waves through disordered media," *Phys. Rev. Lett.*, vol. 61, pp. 2328–2331, Nov. 1988.
[17] I. Freund, "Looking through walls and around corners," *Phys. A, Stat. Mech. Appl.*, vol. 168, no. 1, pp. 49–65, Sep. 1990.
[18] T. J. Schulz and D. L. Snyder, "Imaging a randomly moving object from quantum-limited data: Applications to image recovery from second- and third-order autocorrelations," *J. Opt. Soc. Amer. A, Opt. Image Sci.*, vol. 8, no. 5, pp. 801–807, 1991.
[19] *Emory University Image Database*. Accessed: Jul. 4, 2020. [Online]. Available: http://www.mathcs.emory.edu/~nagy/RestoreTools/
[20] D. Ancora *et al.*, "Phase-retrieved tomography enables mesoscopic imaging of opaque tumor spheroids," *Sci. Rep.*, vol. 7, no. 1, Dec. 2017, Art. no. 11854.
[21] J. Miao, R. L. Sandberg, and C. Song, "Coherent X-ray diffraction imaging," *IEEE J. Sel. Topics Quantum Electron.*, vol. 18, no. 1, pp. 399–410, May 2011.
[22] J. N. Clark, X. Huang, R. Harder, and I. K. Robinson, "High-resolution three-dimensional partially coherent diffraction imaging," *Nature Commun.*, vol. 3, no. 1, pp. 1–6, Jan. 2012.
[23] K. Choi and A. D. Lanterman, "An iterative deautoconvolution algorithm for nonnegative functions," *Inverse Problems*, vol. 21, no. 3, p. 981, 2005.
[24] I. Csiszár and P. C. Shields, "Information theory and statistics: A tutorial," *Commun. Inf. Theory*, vol. 1, no. 4, pp. 417–528, 2004.
[25] E. Isaacson and H. B. Keller, *Analysis of Numerical Methods*. Chelmsford, MA, USA: Courier Corporation, 2012.
[26] L. A. Shepp and Y. Vardi, "Maximum likelihood reconstruction for emission tomography," *IEEE Trans. Med. Imag.*, vol. 1, no. 2, pp. 113–122, Oct. 1982.
[27] D. L. Snyder, T. J. Schulz, and J. A. O'Sullivan, "Deblurring subject to nonnegativity constraints," *IEEE Trans. Signal Process.*, vol. 40, no. 5, pp. 1143–1150, May 1992.
[28] S. Chaudhuri, R. Velmurugan, and R. Rameshan, *Blind Image Deconvolution*. Cham, Switzerland: Springer, 2014.
[29] D. Ancora *et al.*, "Optical projection tomography via phase retrieval algorithms," *Methods*, vol. 136, pp. 81–89, Mar. 2018.
[30] S. Preibisch *et al.*, "Efficient Bayesian-based multiview deconvolution," *Nature Methods*, vol. 11, no. 6, p. 645, 2014.
[31] K. Choi and A. D. Lanterman, "Phase retrieval from noisy data based on minimization of penalized i-divergence," *J. Opt. Soc. Amer. A, Opt. Image Sci.*, vol. 24, no. 1, pp. 34–49, 2007.
[32] T. Wu, O. Katz, X. Shao, and S. Gigan, "Single-shot diffraction-limited imaging through scattering layers via bispectrum analysis," *Opt. Lett.*, vol. 41, no. 21, pp. 5003–5006, 2016.
[33] T. Wu, J. Dong, and S. Gigan, "Non-invasive single-shot recovery of a point-spread function of a memory effect based scattering imaging system," *Opt. Lett.*, vol. 45, no. 19, pp. 5397–5400, 2020.
[34] E. Engel and R. M. Dreizler, *Density Functional Theory* (Theoretical and Mathematical Physics). Berlin, Germany: Springer, 2011.
[35] J. Fienup and C. Wackerman, "Phase-retrieval stagnation problems and solutions," *J. Opt. Soc. Amer. A, Opt. Image Sci.*, vol. 3, no. 11, pp. 1897–1907, 1986.

Daniele Ancora received the B.S. and M.S. degrees from the Department of Physics, La Sapienza Università di Roma, and the Ph.D. degree from the Department of Material Science and Technology, University of Crete. During this period, he was a Marie Curie Early Stage Researcher (MSCA-ITN, g.a.: 317526) at the Foundation for Research and Technology Hellas (IESL-FORTH). He held a postdoctoral position with the Institute of Nanotechnology, Consiglio Nazionale delle Ricerche (CNR-NANOTEC), Rome. He is currently running a Marie Curie Individual Fellowship (MSCA-IF, g.a.: 799230) as a Post-Doc at the Department of Physics, Politecnico di Milano. His research interests span from disordered photonics to biomedical optics in diffusive regime at the interface between computational, theoretical, and experimental imaging.

Andrea Bassi received the Ph.D. degree in physics from the Politecnico di Milano in 2006. He conducted research at the Beckman Laser Institute, University of California (Irvine), as a Research Specialist (2005–2006); also at the Politecnico di Milano as a Tenured Researcher (2009–2014); and also at the Max Planck Institute of Molecular Cell Biology and Genetics (Dresden) as a Marie Curie Fellow (2013–2014). He is currently an Associate Professor with the Department of Physics, Politecnico di Milano. His scientific interests include optical tomography and microscopy for biological and preclinical applications.